Migration of DNA Due to a Combination of Parallel Pressure Gradient and External Electric Field

Shujun He

Ryan J. Montes, Jason E. Butler, Dmitry I. Kopelevich

Department of Chemical Engineering,

University of Florida, Gainesville, FL 32611-6005

ABSTRACT

A combination of a parallel electric field and pressure gradient can cause DNA molecules to migrate transverse to the field lines. We hypothesize that the phenomenon is due to an electrically induced velocity disturbance. A Brownian dynamics method for a bead-spring model of a polymer, that incorporates this electrically induced velocity disturbance, was constructed and used to predict the dynamics of DNA molecules transported through a microfluidic channel due to the pressure driven flow and electric field. Using simulation, we obtained the probability distribution of the centers-of-mass of the DNA molecules in multiple channels with different cross-sectional dimensions. Preliminary simulation results match, at least qualitatively, the extent of migration and the entry length measured in the experiments.

I. INTRODUCTION

Experimental results have shown that pressure driven DNA in confined space undergoing electrophoresis can migrate transverse to the fields lines [1]. The ability to control transverse migration of DNA has applications in biotechnology such as biosensing, genomic mapping, and lab-on-chip devices.

The literature has claimed viscoelasticity can cause migration [2], and it has also been proposed that a long range electrically induced velocity disturbance is the reason for DNA migration [3]. The latter theory predicts that the DNA is first extended and aligned at an angle with respect to the channel axis by the shearing flow, and then the electric field generates a net transverse migration caused by the electrically induced velocity disturbance. An electro-hydrodynamic tensor is used to account for the disturbances caused by electro-hydrodynamic interactions [3], and the Rotne-Proger tensor is used to approximate the hydrodynamic interactions [4]. We extend the model proposed by Kekre *et al.* [3] to better fit experiments performed in the same lab, with different variables such as channel dimensions, electric field strength, and mean shear rate. We present simulation results with different conditions, and compared extents of migration across different conditions. We also analyzed the radius of gyration tensor to better understand the configuration of the DNA molecule as it migrates. Ultimately, we seek to predict the optimal conditions to achieve maximum

DNA migration.

II. SIMULATION METHODS

A. Model

The DNA molecules are modeled as a chain of beads connected by springs. Each bead i in this bead-spring model of the DNA is governed by a force balance

$$\mathbf{F}_i^D + \mathbf{F}_i^S + \mathbf{F}_i^R + \mathbf{F}_i^B + \mathbf{F}_i^W = 0, \tag{1}$$

where inertia has been ignored. The forces are drag, spring, repulsive, Brownian, and wall repulsive forces, reading left to right in equation (1). Each of the forces is described in the following paragraphs.

The drag force is

$$\mathbf{F}_i^D = \zeta[\frac{d\boldsymbol{r}_i}{dt} - \boldsymbol{u}_i^\infty], \tag{2}$$

where $\zeta = 6\pi\eta a$ is the drag coefficient and $\boldsymbol{u}_i^\infty$ is the disturbance velocity evaluated at the center of the bead i. Note that η is the viscosity of the fluid and a the radius of the bead.

For the DNA (Zimm) model, we use FENE springs, which has a potential of [4]

$$\Phi^S(r_{ij}) = -\frac{1}{2}\kappa r_0^2 \ln\left(1 - \frac{r_{ij}^2}{r_0^2}\right), \tag{3}$$

where κ is the spring constant, r_0 is the maximum allowed extension of a spring, and r_{ij} is the bond length between bead i to bead j. So the FENE spring force is then

$$\mathbf{F}_i^S = \frac{\kappa \boldsymbol{r}_{ij}}{1 - \frac{r_{ij}^2}{r_0^2}}. \tag{4}$$

Additionally, we considered the Rouse model for validation, where the Hookean spring force is used

$$\mathbf{F}_i^S = \kappa \boldsymbol{r}_{ij}. \tag{5}$$

To prevent beads from overlapping, we introduce an excluded volume repulsive force between beads with potential [4],

$$\Phi^R(r_{ij}) = A\exp(-\beta r_{ij}^2). \tag{6}$$

The corresponding force is

$$\mathbf{F}_i^R = 2A\beta \exp(-\beta r_{ij}^2)\boldsymbol{r}_{ij}. \tag{7}$$

The wall force is similar to the excluded volume force, but is twice as large in magnitude.

The Brownian force satisfies the fluctuation-dissipation theorem [5]

$$\langle \mathbf{F}_i^B(t) \rangle = 0, \tag{8}$$

$$\langle \mathbf{F}_i^B(t)\mathbf{F}_j^B(t_0) \rangle = 2k_BT(\boldsymbol{\mu}_{ij}^{RP})^{-1}\delta(t-t_0), \tag{9}$$

where k_BT is the Boltzman energy term, $\boldsymbol{\mu}_{ij}^{RP}$ the mobility tensor, and δ the Dirac delta function.

We use the Rotne-Proger (RP) tensor, $\boldsymbol{\mu}^{\boldsymbol{RP}}$, to describe the hydrodynamic interactions between individual beads; the RP tensor $\boldsymbol{\mu}_{ij}^{\boldsymbol{RP}}$ is [4]

$$\boldsymbol{\mu}_{ij}^{\boldsymbol{RP}} = \frac{1}{6\pi\eta a} \begin{cases} C_1\mathbf{I} + C_2\dfrac{\boldsymbol{r}_{ij}\boldsymbol{r}_{ij}}{r_{ij}^2}, & r_{ij} \geq 2a, \\ C_1'\mathbf{I} + C_2'\dfrac{\boldsymbol{r}_{ij}\boldsymbol{r}_{ij}}{r_{ij}^2}, & r_{ij} < 2a, \\ \mathbf{I}, & i = j, \end{cases} \tag{10}$$

where

$$\begin{aligned} C_1 &= \frac{3}{4}\frac{a}{r_{ij}} + \frac{1}{2}\frac{a^3}{r_{ij}^3}, \; C_2 = \frac{3}{4}\frac{a}{r_{ij}} - \frac{3}{2}\frac{a^3}{r_{ij}^3}, \\ C_1' &= 1 - \frac{9}{32}\frac{r_{ij}}{a}, \quad C_2' = \frac{3}{32}\frac{r_{ij}}{a}. \end{aligned} \tag{11}$$

Upon adding an electric field and an ambient flow field, the differential equation becomes

$$\frac{d\boldsymbol{r}}{dt} = [\boldsymbol{u}^\infty + \boldsymbol{\mu}^{\boldsymbol{RP}} \cdot (\mathbf{F} + \mathbf{F}^B) + \boldsymbol{\mu}^{\boldsymbol{E}} \cdot \mathbf{F}^E], \tag{12}$$

where $\boldsymbol{r}$ is the vectorized positions of all beads, $\mathbf{F}$, $\mathbf{F}^B$, and $\mathbf{F}^E$ are the vectorized forces, and $\boldsymbol{\mu}^{\boldsymbol{RP}}$ and $\boldsymbol{\mu}^{\boldsymbol{E}}$ are the grand mobility tensors for the hydrodynamic interactions and electrically induced fluid disturbances. The electric force is

$$\mathbf{F}_i^E = Q\boldsymbol{E}, \tag{13}$$

where Q is the charge carried by each bead and $\boldsymbol{E}$ is the electric field strength. We use a simple shear flow, a parabolic flow, and several 3-D pressure driven flows in our simulation. The simple shear is defined as

$$u_x^\infty = \bar{\gamma}(r_y - r_y^{COM}), \tag{14}$$

where $\bar{\gamma}$ is the mean shear rate, and r_y is the y coordinated the bead. The unidirectional pressure driven flow is parabolic,

$$u_x^{\infty} = 2\bar{\gamma}(r_y - r_y^2/h). \tag{15}$$

The 3-D parabolic flows for the square and rectangular channel grids are obtained numerically and the flow field velocity for each bead is interpolated using the 4 adjacent grid points.

The electrophoretic mobility is [3]

$$\boldsymbol{\mu}_{ij}^{\boldsymbol{E}} = \begin{cases} \frac{\lambda_D^2}{4\pi\eta a^3 {r_{ij}}^3}\left[\frac{3\boldsymbol{r}_{ij}\boldsymbol{r}_{ij}}{{r_{ij}}^2} - \mathbf{I}\right], & r_{ij} \geq 2a, \\ 0 & r_{ij} < 2a, \\ \mu_0^E \mathbf{I}, & i = j, \end{cases} \tag{16}$$

where $\tilde{\mu}_0^E = 0.514$ is the unsheared electrophoretic mobility, and λ_D is the Debye length.

B. Numerical Methods

All forces and flows are calculated based upon the instantaneous positions of the DNA beads, and the stochastic Brownian displacements are calculated using a uniformly distributed random number generator that has a mean of zero and variance of 1/12. More specifically, the Brownian force meets the following condition

$$\langle \mathbf{F}_i^B(t)\mathbf{F}_j^B(t_0)\rangle = 2k_BT(\boldsymbol{\mu}_{ij}^{RP})^{-1}/\Delta t. \tag{17}$$

Therefore, the vectorized Brownian force can be written as

$$\mathbf{F}^B(t) = c\mathbf{B}\cdot\mathbf{W}, \tag{18}$$

where $c = \sqrt{24k_BT/\Delta t}$, $\mathbf{B}$ is the Cholesky decomposition of the RP tensor, and $\mathbf{W}$ is a vector containing uncorrelated random numbers with a mean of 0 and variance of 1/12. The bead velocities are calculated using equation (10), and the velocities are integrated to give their positions as a function of time. An Euler method is used to perform the integration of the stochastic equation, which requires applying a correction for the drift velocity that results from integrating the stochastic portion of the equation of motion [6]. However, the

correction, which is proportional to the divergence of the mobility tensor $\boldsymbol{\mu}_{ij}^{RP}$, is zero in the present case.

The simulations were performed with a time step of 10^{-3}, and the results were confirmed to be convergent, since results, such as radius of gyration and Rouse relaxation times, calculated from simulation data with time steps of 10^{-3} and 10^{-4} were consistent with each other. From the positions as a function of time for a large number of polymer trajectories, averaged quantities such as relaxation time and center-of-mass distributions were calculated. First the simulation method was verified against known results (see section III), and then the simulation was used for calculating the motion of polyelectrolytes in microfluidic channels (see section IV).

III. VALIDATION

Several static and dynamic properties were calculated and compared with the literature to validate our simulation. In the following sections, we list our parameters used and compare our results with those from the literature. Overall, our simulation results closely match those from the literature, validating our simulation.

A. Rouse Model

The Rouse model simulates polymer chains with N identical beads that only experience Hookean spring forces, Brownian forces, and drag forces. The Rouse model assumes no hydrodynamic interaction, so $\boldsymbol{\mu}_{ij}^{RP}$ is replaced by $\mathbf{I}/\zeta$. Non-dimensionalization factors for the Rouse model are summarized in Table I; the only two parameters manipulated were the number of beads N, and the spring constant κ.

Energy	Length	Time
k_bT	a	$\zeta * a^2/k_bT$

Table I. Rouse model non-dimensionalization factors.

To validate our Rouse model, we compared the Rouse relaxation time, τ_r, obtained from simulation results to the analytical solution provided by Doi and Edwards [5]. The analytical

solution is given by the equation

$$\tau_r = \frac{\zeta N^2 b^2}{3\pi^2 k_B T}, \tag{19}$$

where $b = \sqrt{3k_bT/\kappa}$ is the equilibrium bond length; theoretical predictions are compared with simulation results obtained by fitting the correlation function

$$P(t) = < \boldsymbol{Z}(t) \bullet \boldsymbol{Z}(0) >, \tag{20}$$

where $\boldsymbol{Z}$ is the end to end vector, to a single exponential

$$A \exp(-t/\tau_r). \tag{21}$$

Our (dimensionless) results for a 11-bead system are summarized in Table II. The results are within 1% of theoretical predictions.

$\tilde{\kappa}$	$\tilde{\tau}_r$ (simulations)	$\tilde{\tau}_r$ (theoretical)
0.125	97 ± 0.5	98.1
0.25	49 ± 0.5	49.0
0.5	24 ± 0.5	24.5

Table II. Rouse relaxation times from simulation compared to the theoretical solutions. Note that since we non-dimensionalize distance with the bead radius a instead of the effective bond length b, $\tilde{\kappa}$ is equal to $3a^2/b^2$. Tilde indicates non-dimensional values.

B. Zimm Model

In the Zimm Model, neighboring polymer beads are connected by FENE springs, and excluded volume effects are included. Additionally, the full Rotne-Proger mobility tensor is used to include hydrodynamic interactions. Non-dimensionalization factors are summarized in Table III, where $b = \sqrt{k_bT/\kappa}$ (not to be confused with the definition in Doi and Edwards [5] where $b = \sqrt{3k_bT/\kappa}$).

Static and dynamic properties are studied and compared with the literature to validate the simulations. Equilibrium end to end distance is calculated as

$$< R_e^2 > = < (\mathbf{r}_N - \mathbf{r}_1)^2 >, \tag{22}$$

Ref	$\tilde{\kappa}$	$\tilde{a}$	$\tilde{r}_0$	$\tilde{A}$	$\tilde{\beta}$
Kekre *et al.* [3]	1	0.36	5.48	2.71	1.5
Ladd *et al.* [7]	1	0.362	5	2.7	1.8

Table III. Non-dimensionalization parameters in the literature

Energy	Length	Time
k_bT	b	$\zeta * b^2/k_bT$

Table IV. Zimm model non-dimensionalization factors

while equilibrium radius of gyration is calculated as

$$< R_g^2 >= \frac{1}{N} \sum_{k=1}^{N} < (\mathbf{r}_k - \mathbf{r}_{mean})^2 > . \tag{23}$$

Both $< R_e^2 >$ and $< R_g^2 >$ from our simulations match those found in the literature as can be seen in Table V [4, 7].

Ref	Our $< R_e^2 > /b^2$	Author's $< R_e^2 > /b^2$	Our $< R_g^2 > /b^2$	Author's $< R_e^2 > /b^2$
Kekre *et al.* [3]	40.11	40.25	6.86	6.89
Ladd *et al.* [7]	44.1	44.2	7.49	7.5

Table V. Equilibrium end to end to distance and radius of gyration compared with those in the literature

By averaging over a long time ($8 * 10^8$ dimensionless time units), we obtained Rouse relaxation times τ_r that are in agreement with Kekre *et al.* [4], Ladd *et al.* [7]. The results are summarized in Table VI.

C. Length-dependent Electrophoresis

We also validate that length-dependent electrophoresis does occur, if the shape of the polyelectrolytes deviates from that of a sphere [3]. The unsheared electrophoretic velocity, U_0^E is independent of the chain length; however, with inclusion of a constant shear, larger systems start to move faster. The increase in electrophoretic velocity is close to linear for small shear rates but plateaus eventually. The electrically induced velocity disturbance

Ref	Our τ_r/t_0	Author's τ_r/t_0
Ladd *et al.* [7]	16.4	16.4
Kekre *et al.* [3]	15.2	15.2

Table VI. Rouse relaxation times compared with those from the literature

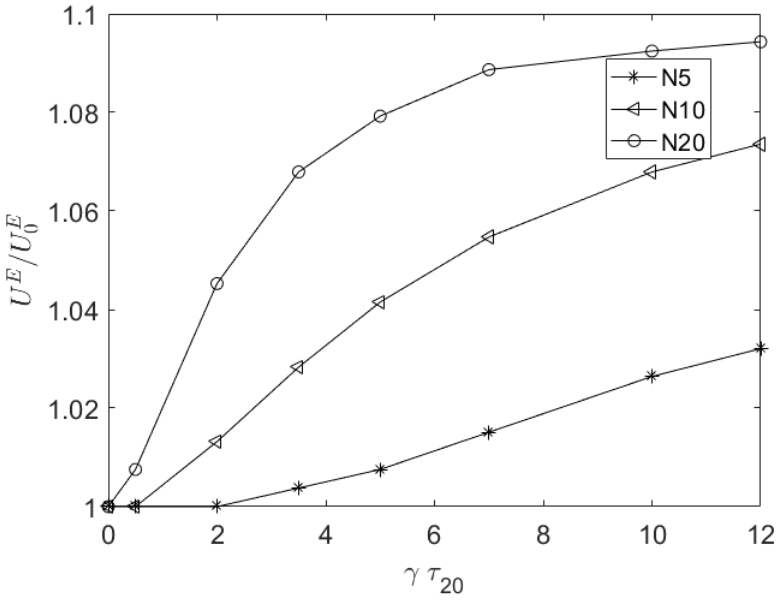

Figure 1. Length-dependent electrophoresis occurs under a constant shear. The electrophoretic velocity is non-dimensionalized by the unsheared electrophoretic velocity, and the shear rate by the viscous relaxation time of a 20-bead system, $\tau_{20} = 16.5$ [3].

generates an additional contribution in the electric field direction upon the extension of polymer under shear [3]. Our results, shown in FIG 1, do not differ more than 2% from Kekre *et al.* [3].

D. Concentration layer thickness and electric field strengths

Theory predicts that at a given mean shear rate, there is an optimal electric field strength that leads to maximum migration [3]. In Kekre *et al.* [3], the 10-bead DNA is confined by two walls with a separation of $100R_g$. We adjusted the electric field strength at a Weissenberg number of $Wi = 0.68$, where Wi is a dimensionless parameter that is the product of the mean shear rate λ and the viscous relaxation time $\tilde{\tau} = 4.57$. We saw that an optimal electric

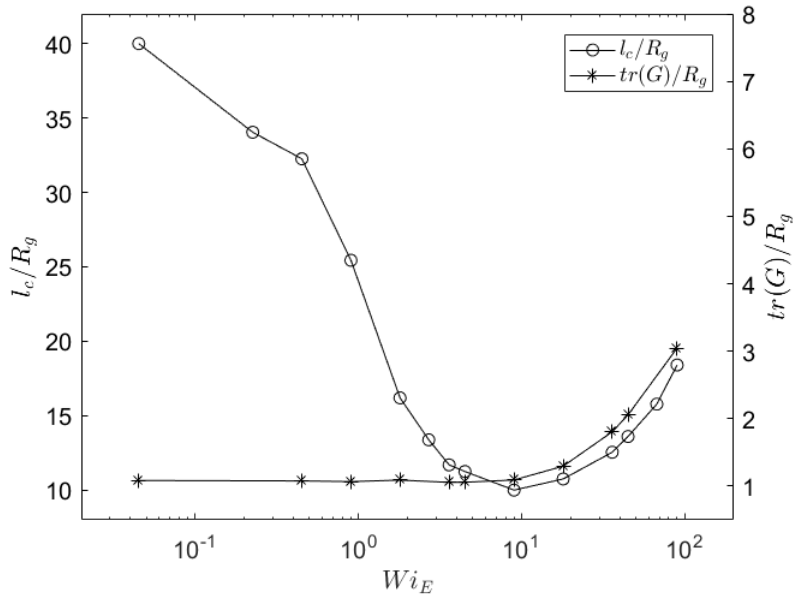

Figure 2. Concentration layer thickness, l_c, nondimensionalized by the equilibrium radius of gyration R_g, is shown to decrease and rebound, upon increase in the electric field strength, E. Trace of the gyration tensor is seen to increase noticeably right after the optimal electric field. The electric field is defined by the electric Weissenberg number $Wi_E = \mu_0^E QE\tau/R_g$, where in dimensionless terms, $\tilde{\mu}_0^E = 0.5143$ and $\tilde{\tau} = 4.57$ [3]. DNA molecules of 20 beads are simulated to obtain results in this figure.

field strength did indeed exist. In FIG 2, the concentration layer thickness, defined as the half width of the area containing 95% of the polymer, decreases to a minimum and then goes back up. Our results are within 3% of the those in Kekre *et al.* [3], which is quite good since Kekre *et al.* [3] does not specify certain parameters. It is evident that at high electric fields, the DNA suddenly becomes large, as shown by the trace of the gyration tensor, and the DNA is further aligned with the field direction, leading to a decrease in migration.

IV. RESULTS

Twenty-bead chains representing λ-DNA undergoing electrophoresis was simulated in a square channel of length 1.8 cm, and the concentration layer thickness is plotted against distance traveled along the channel. Non-dimensionalization factors are the same as those listed in Table IV. A 3-D representation of the evolution of concentration profile is included

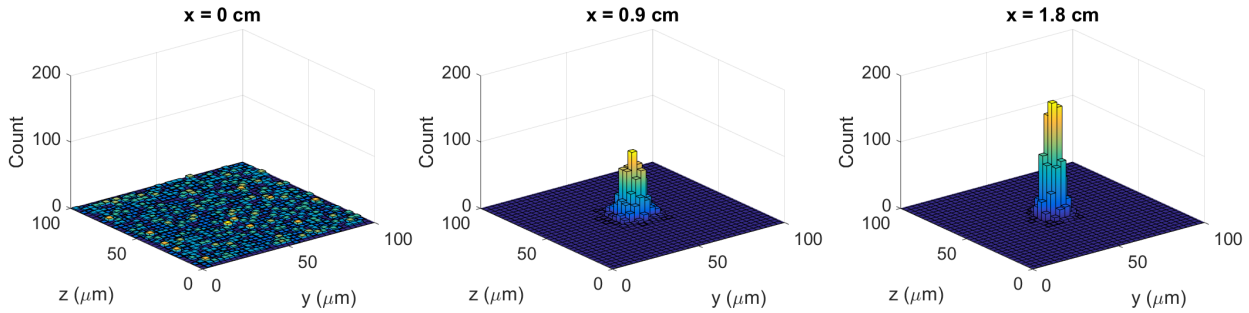

Figure 3. DNA becomes highly concentrated as it travels through the channel. By the exit of the channel, the profile is fully developed. The fields used are characterized as $U_{centerline} = 600$ μm/s and $U_{electrophoretic} = 85$ μm/s.

as well in FIG 3. To better understand DNA migration, we calculated $< 2G_{xx} - G_{yy} - G_{zz} > /R_g^2$, which measures extension of the DNA molecules in the flow direction. In FIG 4, simulation results tell us that initially, DNA molecules are highly extended, leading to a high migration velocity indicated by the steep slope of the l_c curve. As the DNA travels further down the channel, it gets more concentrated in the center, where the shear rate is lower and becomes zero at the exact center of the channel. The DNA extension therefore decreases and migration slows down. As the concentration profile becomes fully developed, $< 2G_{xx} - G_{yy} - G_{zz} > /R_g^2$ drops below 3, suggesting that the DNA reverts back to almost a spherical shape. FIG 4 indicates an entry length of around 1.25 cm, which is consistent with experimental measurements.

We also simulated λ-DNA in a rectangular channel of dimensions 100 μm by 400 μm with an electric field and 3-D pressure driven flow. Evolution of the concentration profile is in FIG 5. Notice that in y (shorter dimension) and z (longer dimension) direction, the extent of migration differs greatly. This is largely due to the fact that the mean shear rate along the z axis is much lower than that along the y axis. The concentration profile is not fully developed by the end of the channel, which is why there are two peaks on the both sides in the third plot in FIG 5. The DNA molecules clustering in those two peaks are experiencing very low shear rate, leading to low migration velocity. Eventually, as the concentration profile becomes fully developed at approximately 120 cm, the two peaks disappear, as can be seen in the fourth plot in FIG 5.

Different electric fields affect the concentration layer thickness differently, as suggested in FIG 6. The optimal electric field strength is different depending on the axis. Coming from

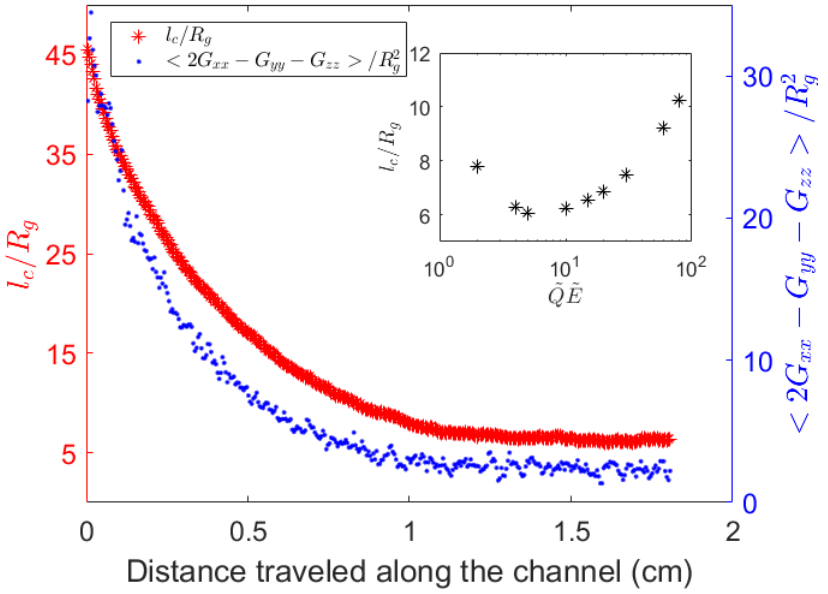

Figure 4. Concentration layer thickness l_c/R_g and $< 2G_{xx} - G_{yy} - G_{zz} > /R_g^2$ are plotted against distance traveled along the channel. Radius of gyration R_g in dimensional terms is approximately 1 μm.

the z axis, the optimal electric field is around $\tilde{Q}\tilde{E} = 30$, whereas from the y axis, the optimal is $\tilde{Q}\tilde{E} = 8$. This is due to the difference in extension in the y and z direction. The polymer is more extended in the y direction because the shear rate is higher. As noted before, the over-extension of DNA leads to further alignment of the DNA in the field direction and decreases migration. The over-extension happens earlier with a higher shear rate, and later with a lower shear rate. In the z direction, the optimal electric field is higher because smaller shear rate leads to over-extension that happens later.

Further, we explored the effects of the pressure field centerline velocity on the extent of migration. Primarily, we wanted to see that if from z direction (wider side), changing the pressure field would give us more migration at the exit of the channel. We found that indeed there is an optimal pressure flow velocity that gives the most migration in FIG 7. Similar to when we vary the electric field, the extent of migration decreases after the optimal pressure field velocity is reached, and extents of migration differs in the y and z direction.

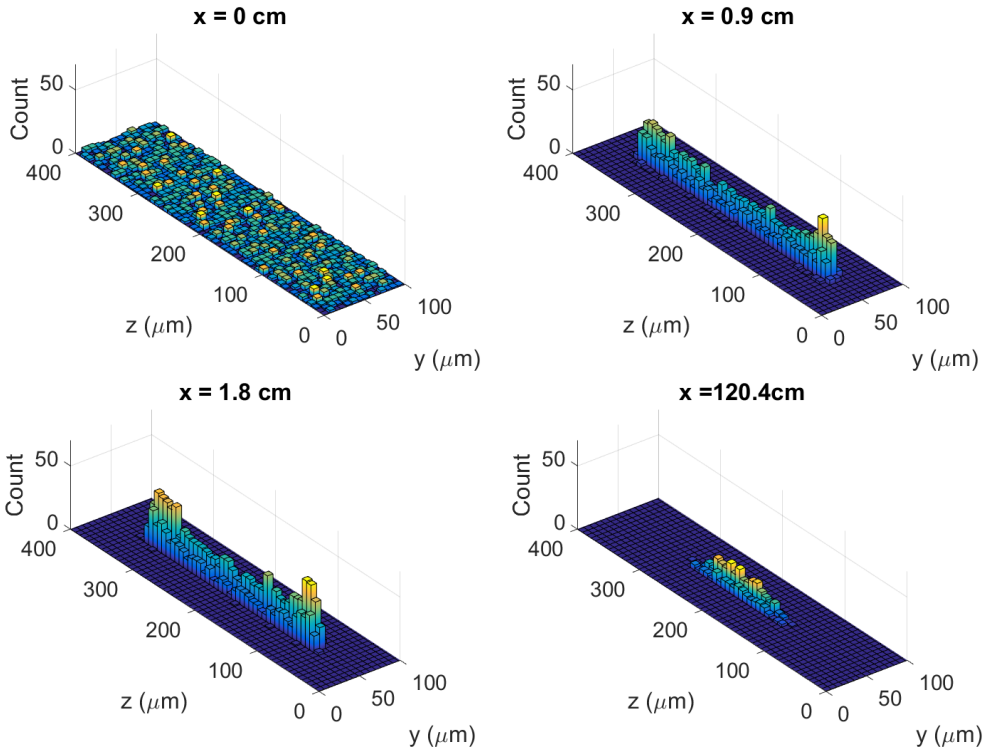

Figure 5. Evolution of the concentration profile of DNA in a rectangular channel is simulated. At the exit of the channel (1.8cm), the profile is far from fully developed. At 1.2 m, DNA becomes concentrated looking from the z axis and the profile is fully developed.

V. CONCLUSION

We conducted simulations using parameters found in existing work and our simulation results match those in the literature quantitatively, validating our work. Our results show that DNA migration under electric and pressure driven flow can be explained by the electrically induced velocity disturbance. The DNA under shear is extended and aligned at an angle, and then the electric field generates a contribution transverse to the field direction. Higher relative extension in the field direction leads to a higher migration velocity, and migration velocity decreases as more DNA migrates to the center of the channel. DNA migration under 3-D pressure flow in a square channel and rectangular are simulated with adjusted parameters to match experimental conditions. We found that not only is there an optimal electric field for a 2-D pressure flow, but also for a 3-D pressure flow. Additionally, adjusting pressure driven flow can lead to more migration. A square channel shows symmetric migration from the y and z direction, while a rectangular channel shows different extents of migration in different directions. Our preliminary results are at least consistent with

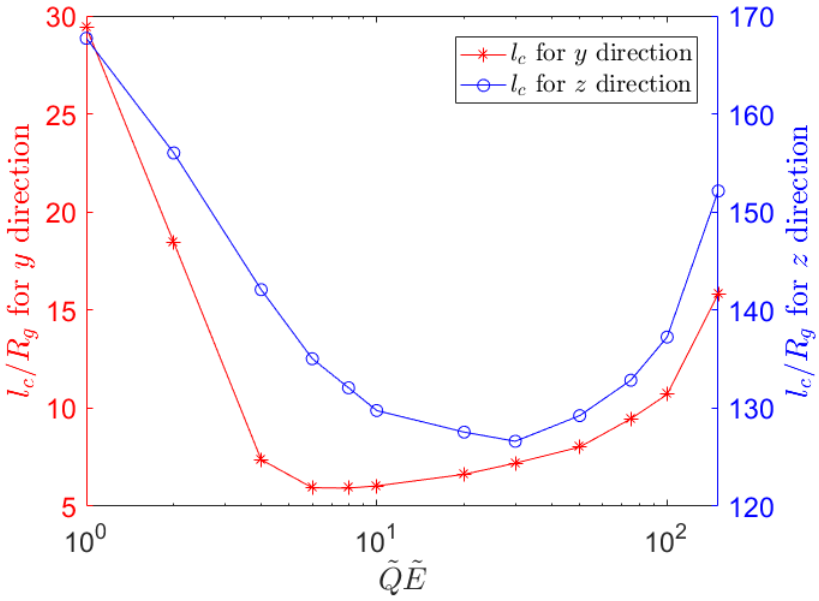

Figure 6. Concentration layer thickness at different electric fields in a rectangular channel is plotted. The center line velocity is $U_{centerline} = 600$ μm/s or $\tilde{U}_{centerline} = 37.23$. Different directions show different optimal electric field strengths that would give maximum migration. Note that since in the z direction, the profile is not fully developed at 1.8 cm, we simply averaged the concentration layer thickness at the exit, while from the y direction, the concentration layer thickness was calculated using fully developed results.

experimental results qualitatively. Extents and rates of DNA migration depend on electric field strength, pressure driven flow velocity, and channel dimensions. In the future, we will compare simulation results to experiments conducted in the same lab in a more quantitative way.

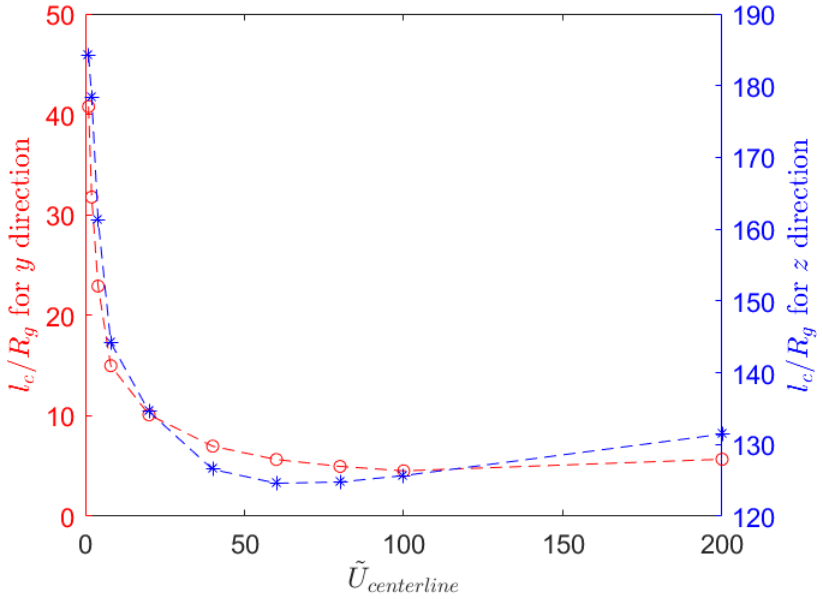

Figure 7. Concentration layer thickness calculated at different pressure flow velocities. The electric field used in this plot is $\tilde{Q}\tilde{E} = 30$.

---

[1] M. Arca, J. E. Butler, and A. J. C. Ladd, Soft Matter **11**, 43754382 (2015).

[2] H. Ranchon, R. Malbec, V. Picot, A. Boutonnet, P. Terrapanich, P. Joseph, T. Leichle, and A. Bancaud, Lab on a Chip **16**, 1243 (2016).

[3] R. Kekre, J. E. Butler, and A. J. C. Ladd, Phys. Rev. E **82**, 050803(R) (2010).

[4] R. Kekre, J. E. Butler, and A. J. C. Ladd, Phys. Rev. E **82**, 011802 (2010).

[5] M. Doi and S. F. Edwards, *The theory of polymer dynamics* (Clarendon Press, 2009).

[6] D. L. Ermak and J. McCammon, J. Chem. Phys. **69**, 1352 (1978).

[7] A. J. Ladd, R. Kekre, and J. E. Butler, Phys. Rev. E. **80**, 036704 (2009).